RESEARCH ARTICLE | SEPTEMBER 25 2025

An experimental study on the spreading and fingering instability of droplet impacting on a surface with plasma discharge

Jorge Ahumada Lazo; Yang Liu

Physics of Fluids 37, 093380 (2025)
https://doi.org/10.1063/5.0291036
CHORUS

Physics of Fluids ARTICLE pubs.aip.org/aip/pof

An experimental study on the spreading and fingering instability of droplet impacting on a surface with plasma discharge

Cite as: Phys. Fluids **37**, 093380 (2025); doi: 10.1063/5.0291036
Submitted: 15 July 2025 · Accepted: 11 September 2025 ·
Published Online: 25 September 2025

Jorge Ahumada Lazo and Yang Liu[a)]

AFFILIATIONS

Department of Mechanical Engineering, The City College of New York, New York, NY 10031, USA

[a)]Author to whom correspondence should be addressed: yliu7@ccny.cuny.edu

ABSTRACT

Droplet impact on a solid surface is a commonly recurring phenomenon in nature and industrial processes. The droplet dynamics and degree of spreading have been extensively studied and are well understood. These processes, however, are substantially altered in the presence of a non-thermal plasma over the solid surface. This study discusses the dynamics of water droplet spreading on the plasma-covered dielectric surface of a dielectric barrier discharge actuator made out of poly (methyl methacrylate). Exposure to plasma modifies the polymer surface, resulting in increased wettability. In addition, plasma lowers the surface tension of water, which results in a higher degree of spreading. In particular, a notable fingering instability develops at the edge of the droplet due to the combined effects of droplet inertia and electrical forces on the droplet. Not only is the droplet morphology affected by the plasma, but the plasma discharge itself conforms to the shape acquired by the droplet. This finger formation has further effects on the subsequent formation of secondary droplets, plasma streamers, and droplet evaporation. The degree of droplet spreading, number of fingers formed, their size, and spacing are evaluated with respect to Weber number ($20 < \mathrm{We} < 500$) and electrical Bond number ($0 \leq Bo_e \leq 2.20$).

NOMENCLATURE

Latin letters

C	Centroid of the droplet
d	Droplet diameter
d_0	Initial droplet diameter
E	Electric field strength
f	Frequency
h	Droplet release height
L	Distance to the electrode edge
l_e	Electrode length
l_f	Finger length
N_m	Most probable mode in entire circumference
n_m	Most probable mode in exposed region
r	Radial coordinate
$\bar{r}$	Average droplet radius
r_0	Initial radius
r_{fb}	Radius to average finger base
r_{ft}	Radius to average finger tip
S	Spreading parameter
t	Time
U	Velocity
V	Voltage
w_e	Electrode width

Greek letters

α	Contact angle
β	Degree of droplet spreading
γ	Interfacial surface tension
ϵ	Emissivity
ε_0	Permittivity of vacuum ($=8.85418 \times 10^{-12}\,\mathrm{m^{-3}\,kg^{-1}\,s^4\,A^2}$)
ε_r	Relative permittivity
θ	Angular coordinate
$\theta*$	Angle of contact with plasma streamer
θ_{fs}	Angular range of finger structures
θ_r	Angular range of exposed liquid
λ	Wavelength
μ	Dynamic viscosity
ρ	Density

σ Liquid surface tension

Non-dimensional numbers

Bo_e Electrical Bond number
Re Reynolds number
We Weber number
Θ Ratio of finger-occupied angular coordinate ($= \theta_{fs}/\theta_r$)

Acronyms

AC Alternating current
DBD Dielectric barrier discharge
FFT Fast Fourier transform
fps Frames per second
IR Infrared
PAW Plasma activated water
PMMA Polymethyl methacrylate
RONS Reactive oxygen and nitrogen species

I. INTRODUCTION

Plasma–droplet interactions have been recognized as the fundamental mechanisms of a wide range of technological processes, including propulsion, material processing, health care, nanomaterial synthesis, and water treatment.[1] These processes usually involve multi-scale multi-physics such as heat and mass transfer, charge transfer, interfacial instabilities, and chemical activations. Many molecular-scale reactions and transport processes of short-lived species occur in these mechanisms, e.g., transport of O–H radicals from gas-phase plasma to liquid-phase droplet,[2] contributing to the complexity of plasma–droplet interactions in different regimes.[3] In recent years, along with the new advancement of plasma-based anti-/deicing technologies[4] and additive manufacturing (AM) and coating technologies,[5] the interactions between plasma discharge and droplets have gained significant attention due to their fundamental roles in determining the practical performances of these multiphase systems.

Although considerable progress has been made in advancing the understanding of plasma–droplet interactions, existing research has predominantly focused on plasma-induced chemical reactions, radical generation, and molecular-level transport phenomena.[2,3,6,7] These efforts have provided valuable insights into the chemistry of plasma–liquid systems; however, fundamental investigations of droplet hydrodynamics under transient conditions remain limited. In particular, the impact of droplets on solid surfaces in the presence of plasma, a process central to many emerging technologies (e.g., plasma-assisted deicing and plasma-based coating and printing methods), has not been systematically examined. The complexity is further highlighted when solid boundaries are incorporated into this multiphase environment, giving rise to coupled plasma–liquid–solid interactions that are largely unexplored. Addressing this gap requires a comprehensive understanding of the hydrodynamic instabilities and transient droplet behaviors upon impinging on surfaces with plasma discharge.

Droplet impact on a solid surface is a ubiquitous phenomenon that has been studied for nearly 150 years since Worthington[8] published his work, where some of the more prominent features of droplet impact, such as branching, breakup, and rebound, were discussed. Since then, numerous studies have been carried out addressing varying aspects of droplet impact under different circumstances, which have resulted in various models for droplet spreading and splashing. Although no single unified theory exists,[9] the droplet impact process is relatively well understood. Comprehensive reviews have been written by Josserand and Thoroddsen,[9] focusing on droplet impact on solid surfaces and by Rein,[10] addressing impacts both on solids and liquid surfaces. In general, droplet impact on a solid surface results in one of three outcomes: spreading, splashing, and bouncing,[9–11] with some sub-categories, namely deposition, prompt splash, corona splash, receding breakup, partial or complete rebound, as detailed in the previous work.[12,13] These processes are governed by both droplet and surface properties.[9] On the droplet side, the dominant influences arise from inertia, surface tension, and viscosity, which are characterized by the Reynolds, Weber, and Ohnesorge numbers. The wettability of the surface (i.e., hydrophilic, hydrophobic, or superhydrophobic) plays a pivotal role in the regime of droplet impact as well as the degree of spreading ($\beta = r_{\max}/r_0$) and splashing. The gas surrounding the droplet can induce internal circulation or oscillations of the droplet.[10] Further, some of the cushioning gas can be entrapped in the liquid upon initial contact with the solid, leading to corona splashing.[9] Chandra and Avedisian[11] authored a comprehensive study on the spreading of heptane droplets on a metallic surface at temperatures ranging from $24\,^{\circ}C$ to the Leidenfrost temperature of the fluid ($=200\,^{\circ}C$). With increasing substrate temperatures, a higher fraction of the liquid vaporizes upon contact due to an increased number of nucleation sites. In addition, at temperatures near the boiling point of heptane ($=96\,^{\circ}C$), an array of radial ridges and dry cells were formed over the receding stage. At temperatures just below Leidenfrost, an evident finger instability developed at the outer rim of the spreading droplet.

The dynamics of this well-understood process are significantly altered when the droplet–solid impact occurs in the presence of plasma. There exists, however, little available literature regarding this impact process. These circumstances are frequently encountered in the aforementioned emerging technologies based on the use of non-thermal plasmas, such as dielectric barrier discharge (DBD) plasmas. In particular, the aerospace community has dedicated particular attention to the implementation of surface DBD plasma actuators for flow control[14–20] due to the induced ionic wind and for deicing applications[21–24] due to their rapid and intense thermal effects. In typical DBD actuators, the plasma discharge occurs along the edge of an exposed electrode and propagates within a thin region (1–2 cm) over a dielectric material, usually quartz or polymers.

The addition of the plasma phase adds multiple layers of complexity to the already dynamic, multiphase interaction. Because of the reactive nature of plasma, a series of interfacial chemical reactions takes place when it interacts with other phases changing their physical properties. For instance, plasmas modify the surfaces of polymers,[25–28] increasing their wettability through two different mechanisms: etching, and ion implantation. Plasma also alters the physico-chemical properties of water[29–31] through a process known as plasma activation. In general, plasma activated water (PAW) has increased electrical conductivity, lower pH, higher density, decreased surface tension, and increased viscosity compared to de-ionized water.[29,31]

A particular feature observed in our previous study on the multiphase interactions within the plasma–liquid–gas–solid system,[32] and which is further addressed in this work, is the development of a fingering instability on the droplet as it spreads over the dielectric surface

during plasma actuation. Our previous work[32] revealed that droplet impact hydrodynamics are strongly influenced by the dynamic/thermal processes during plasma discharges, which, in turn, modify the discharge modes and lead to intense localized heating, enhanced evaporation, and alterations in the induced gas flow field. Such interactions create a highly complex environment in which plasma dynamics, interfacial instabilities, and droplet spreading behaviors are strongly interdependent. In particular, the observed fingering patterns reflect the sensitive interplay between transient droplet hydrodynamics, plasma-induced dynamic/thermal processes, and plasma-modified surface properties, highlighting the inherently multiphysics nature of this problem. Despite these observations, systematic investigations of plasma-modulated droplet instabilities during impact remain lacking.

The study of rippling or fingering produced by spreading droplets impacting solid surfaces (in the absence of plasmas) has attracted much attention in the past decades. Marmanis and Thoroddsen[33] investigated the characteristics of the footprint or splatter left after impact of droplets of different liquids with a solid surface (in their case, a thick, porous paper) at relatively high Re (up to $\sim 25\,000$) and We (up to ~ 4000). The formation of finger structures was reported for moderate values of Re, with the number of fingers and finger slenderness increasing with impact velocity. The degree of droplet spreading and the number of fingers were scaled with respect to an *Impact Reynolds number* given by

$$Re_I = \frac{U}{\sqrt{\nu}} \left(\frac{\pi^2 \rho d^3}{16\,\sigma} \right)^{1/4} \propto Re^{1/2}\, We^{1/4}, \tag{1}$$

which considers the characteristic time of impact approximated by the natural free-oscillation period. In a later paper, Thoroddsen and Sakakibara[34] presented an in-depth analysis of the fingering instability of spreading water droplets ($Re \sim 15000$ and $We \sim 1000$) on a hydrophilic glass surface. Intricate phenomena present during spreading, such as finger splitting and merging, were described and attributed to capillary waves in the azimuthal direction. It should be noted that the structures described by Thoroddsen and Sakakibara correspond to the small amplitude ripples observed in our experiments in the absence of plasma. Certain inhomogeneities, such as roughness of the solid surface, entrapment of air bubbles, and phase changes, may trigger the instability of the spreading rim.[35] Beautifully intricate jetting and finger structures were produced by Zhang *et al.*[36] in an experimental study using compound droplets of water–glycerin as the continuous phase containing smaller immiscible droplets of perfluorohexane.

Plasma-induced finger instabilities at the liquid–air (LA) interface have been observed in Helle-Shaw cell experiments,[37–40] exhibiting similarities to the classical Saffman–Taylor instability.[41] Chu and Lee[37] first reported the formation of finger structures on the interface of an air bubble and a silicone oil confined in a cell of 0.4 mm in thickness upon plasma ignition within the bubble. With continuous plasma actuation, the fingers branched and formed fractal patterns. In the radial fingering phase, the wavelength (λ) was found to be insensitive to bubble size but varied with gap size (d) and liquid viscosity (μ) as $\lambda \propto d\mu^{-0.5}$. In the fractal branching regime, the fractal dimension of expansion was found to be consistent with known values for the Saffman–Taylor instability in Newtonian fluids. In a later paper by Hou and Chu,[38] similar finger and branching evolutions were found under different interface configurations: bubble, channel, and droplet. In all configurations, localized plasma discharges were observed at the fingertips of the gas phase.

In this work, we present a detailed analysis of fingering development during droplet impacts in the presence of plasma discharges. Our study reveals stark contrasts in the onset, growth, and morphology of fingering instabilities compared to impacts on plasma-free surfaces. These findings not only provide new physical insights into the coupling between plasma actuation and droplet impinging dynamics but also establish a foundation for rationally controlling interfacial instabilities in plasma-assisted technologies. In the context that follows, a description of the experimental methods and data analysis was provided. Then, the experimental results are presented where the inertial and plasma-induced effects on the finger structures are discussed. This is followed by further discussions and concluding remarks.

II. METHODS

A. Experimental setup

The experimental setup is schematically shown in Fig. 1(a). Single droplets of distilled water were generated at a variable height h above the surface of a typical DBD actuator using a syringe pump (NE-1000, New Era Pump Systems, Inc., Farmingdale, NY) through a stainless-steel needle. The distance L between the droplet impact location and the edge of the electrode was adjusted for the two droplet sizes to ensure the droplet wetted the electrode during the spreading phase even in the absence of electrical stresses. In this study, the normalized L/d was maintained between 0.8 and 1.2.

The DBD actuator used in this study consisted of two electrodes: one exposed to the air, and the second one encapsulated by the dielectric material. Figure 1(b) offers a top view of the actuator with its relevant dimensions as well as a representation of the finger instability developed on the droplet as it spreads over the dielectric material. The electrodes were made out of copper tape of thickness $t_e = 0.05$ mm, the width and length of the electrodes were $w_e = 25.4$ mm, and $l_e = 60$ mm, respectively. The electrodes were positioned asymmetrically so that there was no gap between them. The dielectric material was polymethyl methacrylate (PMMA or acrylic) with a thickness of 5.25 mm between the two electrodes. The top surface of the PMMA was coated with a black spray paint to improve the emission properties of the acrylic for the purposes of infrared (IR) imaging. The wetting properties of both actuator materials were determined by measuring the static contact angle of a water droplet for an untreated surface, a plasma-treated surface, and well as the advancing contact angle during plasma actuation. The results are presented in Table I.

The two electrodes were connected to a high-voltage AC source (CTP-2000K, Nanjin Suman Plasma Technology Co., LTD) to generate a non-equilibrium plasma discharge on the surface of the dielectric material. The power supply provided a high-voltage sinusoidal signal of controllable voltage and frequency. For the current study, the AC frequency was fixed at $f = 10$ kHz.

Thermal infrared (IR) and high-speed (HS) images were simultaneously recorded, offering a top view of the actuator in the experiment. The IR (FLIR A600-Series, FLIR, Täby, Sweden) and HS (FASTCAM Nova R3-4K, Photron USA, Inc., San Diego, CA) cameras were synchronized and controlled through a delay/pulse generator. The IR images were acquired at a frame rate of 200 fps with a spatial resolution of 640×120 pixels, yielding a magnification of 0.24 mm per pixel. The camera was controlled, and images were processed with the software

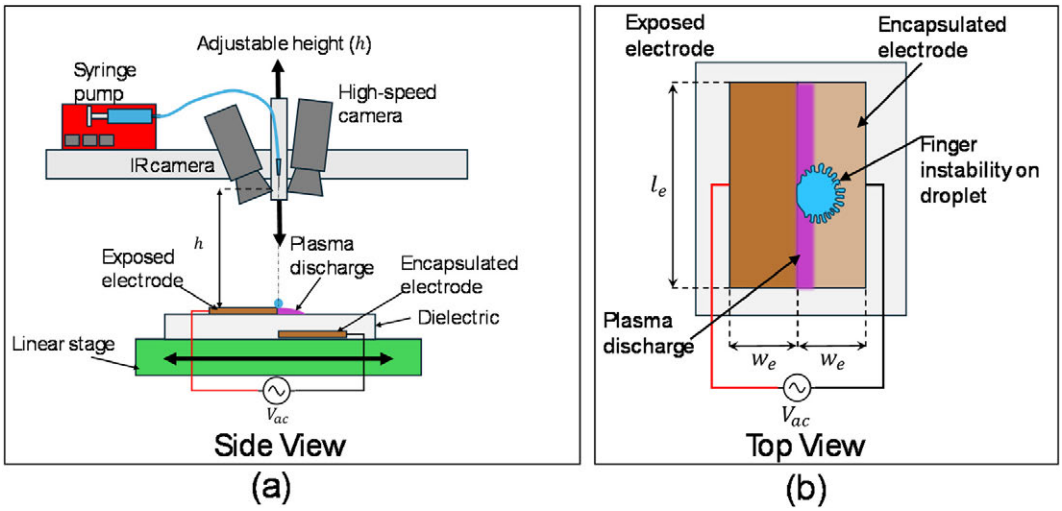

FIG. 1. (a) Schematic of the experimental setup. (b) Schematic and dimensions of the surface DBD actuator.

IR research (FLIR, Täby, Sweden). Temperature was obtained by calibrating the camera according to the working distance and the emissivity of the black plaint on the dielectric surface ($\epsilon = 0.95$). The HS camera was operated at 3000 fps with a resolution of 20.44 μm per pixel. A UV lens (UV-Nikkor 105 mm F4.5, Nikon, Japan) with a high transmittance rate (~70%) was attached to the camera to capture plasma structures. Both cameras were mounted on adjustable optical rails and carefully aligned such that their optical axes intersected at the droplet impact center, minimizing perspective mismatch. The IR camera was positioned at a slight angle relative to the surface normal to avoid direct reflection, while the high-speed camera was oriented perpendicularly. To correct for potential perspective artifacts, we performed a calibration procedure prior to the experiments. A calibration target with known (wire) grid dimensions was imaged by both cameras under the same configuration, and the resulting images were used to generate a projective transformation matrix. This transformation was then applied to the recorded experimental data to correct for geometric distortion and ensure accurate spatial correspondence between the IR and high-speed camera views.

B. Experimental matrix

The experimental matrix comprised 32 combinations given by two needle sizes (gauges 14 and 25), four release heights, and three plasma intensities, plus a control case without plasma. The smaller needle (gauge 25) produced droplets of ~1.75 mm in diameter, whereas the larger needle (gauge 14) generated droplets with a diameter of ~3 mm. For each needle size, four heights (h) were evaluated: 5, 20, 40, and 60 cm. This resulted in a range of We from 20.44 to 490.5 following Eq. (2).

TABLE I. Contact angle measurements of actuator materials.

Material	Static CA untreated surface	Static CA treated surface	Advancing CA plasma actuation
Painted PMMA	69.1°	25.7°	14.8°
Copper tape	56.3°	36.6°	30.9°

$$We = \frac{\rho U^2 d}{\sigma}. \tag{2}$$

The peak-to-peak voltages applied to each combination of droplet size and h described above were 0 V (no plasma), 13.28, 24.6, and 29.8 kV. This resulted in electric fields of 0 V/m, 1.207×10^5 V/m, 2.236×10^5 V/m, and 2.709×10^5 V/m, respectively, based on the signal amplitude and the thickness of the dielectric material. The electric field strength was used to calculate Bo_e using Eq. (3), which yielded a range from 0.21 to 2.19, considering both droplet sizes.

$$Bo_e = \frac{E^2 \varepsilon_0 \varepsilon_r d}{\gamma}. \tag{3}$$

The droplet spreading profile for each case is shown in Fig. 2 for (a) $d_0 = 1.75$ mm and (b) $d_0 = 3$ mm. It becomes evident that both inertial and electrical effects play a role in the droplet spreading and the formation of finger structures. The following section describes the procedure followed to quantify the morphological features of the droplet profiles shown in Fig. 2. These properties are then discussed with respect to the non-dimensional parameters of interest Bo_e and We.

C. Data analysis

As revealed in Fig. 2, the fingers within a single droplet display great variability in length, slenderness, and direction. In some instances, two or more fingers merge during spreading, leading to irregularly shaped structures. Thus, as accurately disclosed by Marmanis and Thoroddsen[33] and by Thoroddsen and Sakakibara,[34] counting the number of fingers can be somewhat subjective. To systematically quantify the fingers and measure finger distribution and length, the following procedure was implemented (and shown in Fig. 3). Thermal images of the spreading droplets were used, taking advantage of the

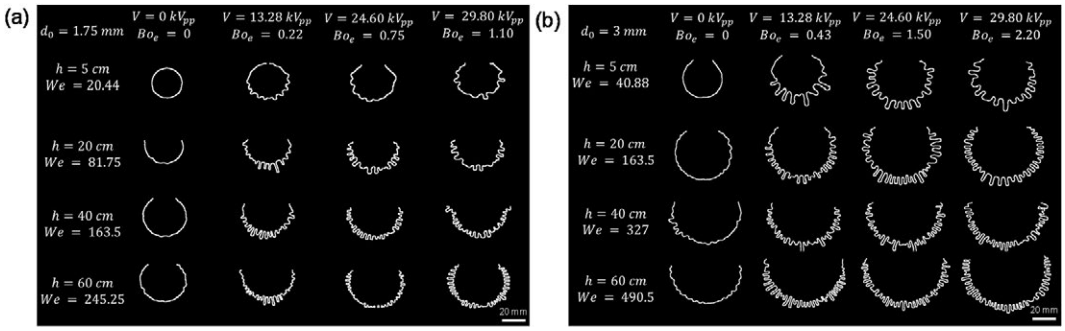

FIG. 2. Processed droplet profiles obtained from thermal imaging for (a) $d_0 = 1.75$ mm and (b) $d_0 = 3$ mm. A notable variation in finger structure length, slenderness, and number of fingers is observed with respect to the non-dimensional parameters of interest Bo_e and We.

high contrast offered over other forms of photography. The image in Fig. 3(a) shows a typical thermal image taken soon after droplet impact (within 5–10 ms). The drastic radiance intensity difference between the droplet and the dielectric surface allows for an easy implementation of an edge detection algorithm. To further facilitate the process, the dynamic range of displayed radiance was adjusted within the IR camera software (ResearchIR, FLIR Systems) to lump the small intensity variations within the droplet into a homogeneous tone.

The image is converted to grayscale, and an x–y coordinate system is defined such that its origin lies at the center of the droplet. The x and y axes run perpendicular and parallel to the electrode edge, respectively. Then, the built-in MATLAB function for edge detection is applied using the Canny method with a relatively low sensitivity. Frame (c) of Fig. 3 shows the isolated edge of the droplet in white against a black background. These data are then converted to polar $(r,\ \theta)$ coordinates. For practical purposes, the following convention is adopted: the positive θ direction is given by the clockwise angle from the positive x-axis with respect to point C as shown in the figure.

Note also that the straight edge of the electrode, clearly distinguished in frames (a) and (b), is omitted in (c), i.e., only the droplet edge is converted into polar coordinates. Two subsets of the θ domain are then defined for further analysis [indicated in frame (d)]. The first is the angular range θ_r, which contains the entirety of the data. Note that when droplets spread contact the electrode as in the case shown in Fig. 3, $\theta_r < 360°$; θ_r then describes the exposed liquid on the dielectric surface, as shown in frame (e) in the polar coordinates. The second angular measurement is herein referred to as the *region of finger structures*, θ_{fs}. Its limits are given by the outer minimum points (valleys) that enclose the first and last finger structures that surpass $\bar{r}$ at their higher point (peaks), as shown in frame (f) where peaks and valleys are highlighted in blue and red, respectively. The average finger length $\bar{l}_f$ is then calculated from

$$\bar{l}_f = \frac{\bar{r}_{peaks}}{\bar{r}_{valleys}}, \tag{4}$$

where $\bar{r}_{peaks}$ and $\bar{r}_{valleys}$ are the average values of the maxima and minima included in θ_{fs}. The shifted data $(r - \bar{r})$ included in θ_{fs} are then analyzed by Fourier transform analysis. Note that shifting is done to eliminate the offset component mode in the Fourier analysis ($n = 0$). Frame (g) of Fig. 3 shows the FFT of the data, showing the first 300 modes, where the most probable mode ($n_m = 17$) is marked in red. The most probable mode n_m provides information on the number of fingers contained within θ_{fs}; however, since θ_{fs} varies from one case to another, a normalized most probable mode which encompasses the entire circumference is defined as:

$$N_m = n_m \times \frac{360}{\theta_{fs}}. \tag{5}$$

Two closely related parameters are the finger spacing $s(°)$ and the wavenumber λ (mm) given by Eqs. (6) and (7), respectively.

$$s = \frac{\theta_{fs}}{n_m}, \tag{6}$$

$$\lambda = \frac{2\pi\,\bar{r}}{N_m}. \tag{7}$$

The finger slenderness is quantified by the nondimensional ratio $\bar{l}_f/\lambda$. Finally, an angular ratio $\Theta = \theta_{fs}/\theta_r$ is introduced to indicate the portion of the exposed droplet affected by the finger instability. These parameters are calculated for each experimental case and are presented with respect to We and Bo_e in the following section.

III. RESULTS AND DISCUSSION

A. Onset and growth of finger instability

Droplet impact on a DBD plasma actuator gives rise to a series of multiphase dynamic and thermal processes. These start with the noticeable finger instability that develops during the droplet spreading and are followed by plasma–liquid interactions at the droplet's surface and conductive heat transfer from the hot dielectric surface. Droplet evaporation begins at the thin finger structures and near the exposed electrode. Plasma streamers unevenly heat the droplet until its complete evaporation.[32] This process is shown in Fig. 4 for a droplet of 3 mm in diameter impacting on the surface of dielectric material (polymethyl methacrylate) of a DBD actuator at a relatively low plasma intensity. It is worth mentioning that the parameters of the early fingering features, such as the quantity and length of the fingers, influence the later processes. Since the liquid takes the role of an extended electrode, the plasma emission is displaced to the outermost parts of the droplet, i.e., the tips of the fingers. These discharges can be seen in Fig. 4 as bright streaks pointing radially out from the fingertips, i.e., in a droplet with pronounced finger structures, the plasma is emitted radially outward, and it is localized exclusively at the fingertips, whereas no plasma discharge occurs in the interstitial space.

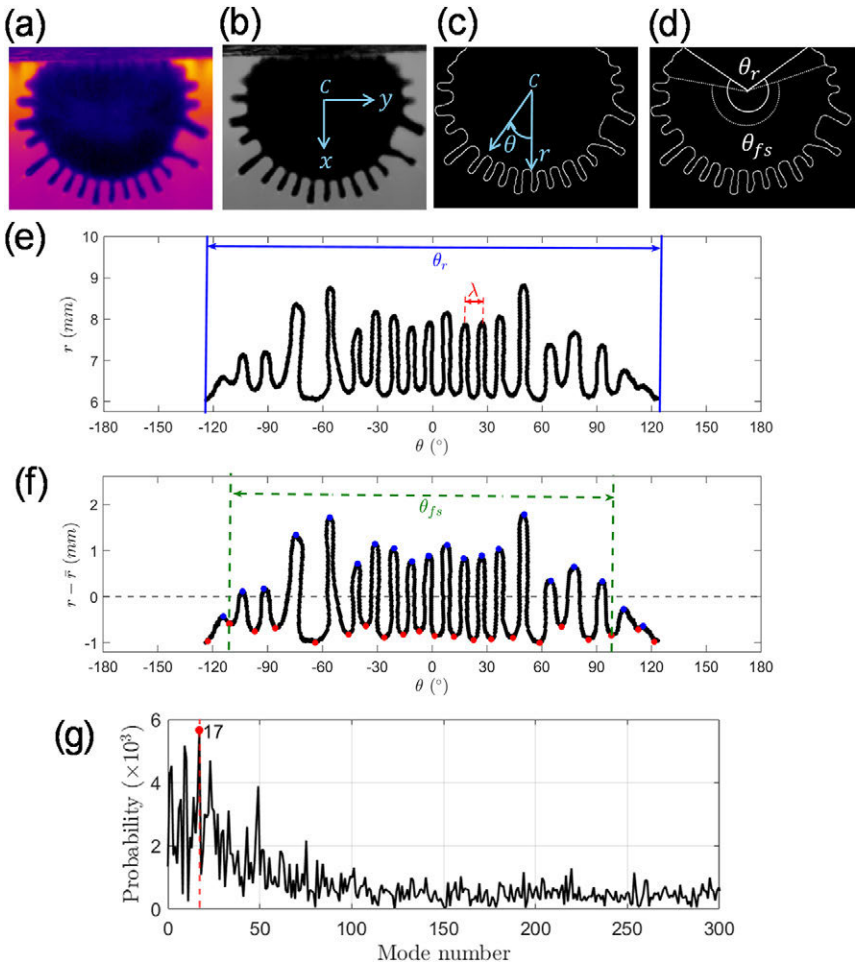

FIG. 3. Methodology for finger instability characterization. (a) Typical thermal image taken within 10 ms of droplet impact. (b) The dynamic range of thermal emissivity is adjusted, and the image is converted to grayscale. (c) Edge detection using Canny's method. A polar coordinate system is shown with the center of the droplet as its origin. (d) Two reference measurements are depicted: the angular range θ_r and the region of finger structures θ_{fs}. (e) The droplet edge is plotted in polar coordinates. The angular range θ_r and wavelength λ are indicated. (f) The polar data are shifted by subtracting the mean droplet radius $\bar{r}$ to eliminate the dc component of the FFT. The local maxima and minima are identified in blue and red, respectively, and θ_{fs} is indicated. (g) FFT of the data contained within the θ_{fs} range. The most probable mode is indicated in red.

The thin fingers heat up more rapidly than other regions, causing liquid evaporation and thermal Marangoni effects, both of which promote a quicker depletion of liquid in the middle. This results in the separation of the fingertips to form secondary droplets. During this process, high-intensity streamers of plasma form between the main and secondary droplets as charges accumulate near the liquid–gas interface and the vapor-saturated air ionizes. These streamers, in turn, add heat and momentum to the adjacent regions of liquid, resulting in a further separation of the secondary droplets from the bulk of liquid. The early formation of streamers is seen in Fig. 4 at $t = 50$ ms. The localized plasma emissions on the fingertips continue, and in fact, intensify with the formation of streamers. The heat emitted by the streamers continues to drive the evaporation of the droplet. This example denotes the impact of the streamer formation on the dynamics of both liquid and plasma phases.

In our experiments, a water droplet is released from a certain height h to impact on the dielectric side of the DBD actuator. In all cases when plasma was present, the advancing rim of the droplet developed into well-defined slender fingers. Furthermore, the same finger features developed even without the droplet contacting the exposed electrode as shown in Fig. 8 and discussed in the following section.

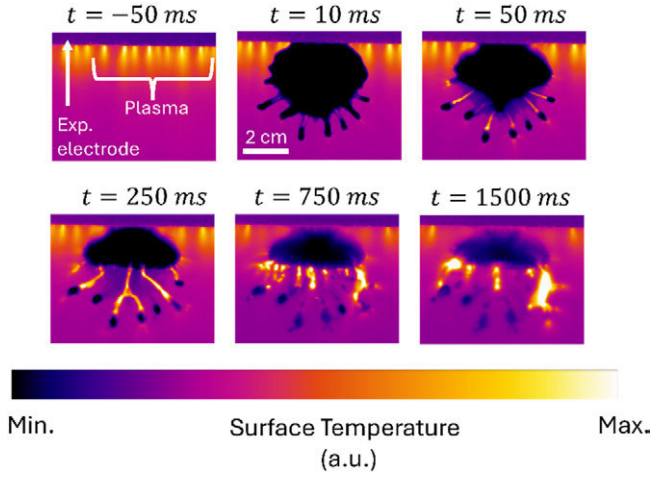

FIG. 4. The sequence of images denotes the separation of thin fingertips to form secondary droplets ($t = 50$ ms). Simultaneously, high-intensity streamers are generated, connecting the primary droplet with the newly formed secondary droplets. These streamers introduce heat to the main droplet and drive its evaporation.

The sequences of photos in Fig. 5 show the droplet impact and spreading over the PMMA dielectric surface of the DBD plasma actuator for the cases with plasma off (a) and plasma on (b). Inspection of the photographs reveals that the finger formation is evident in the presence of plasma. The inner (d_{in}) and outer (d_{out}) diameters of the droplets are approximated with the red and blue superimposed circles, respectively. When the plasma is off, the droplet spreading upon impacting is a typical deposition type under the low *We* number condition, i.e., $We = 250$. Very limited fingering formation was observed, as shown in the snapshots in Fig. 5(a) from $t = 1.5$ ms and $t = 3$ ms. Rapidly after the initial finger formation upon impact, these finger features remain unchanged as can be seen from $t = 3$ ms to $t = 7$ ms. For the case of plasma-on, however, much more evident finger formation was observed upon droplet impacting, although the *We* number was kept the same as that in the plasma-off case. With the emergence of the finger structures, they continuously grow as time goes by, as seen in Fig. 5(b) from $t = 1.5$ ms to $t = 7$ ms.

The time evolution of d_{in} and d_{out} normalized by d_o as well as the normalized average finger length ($l_f = (d_{out} - d_{in})/d_o$ in black triangles) are shown in Figs. 6 and 7, respectively. It is noted from these two plots that in both cases the fingers appear 1.25 ms after impact, as the rim of the droplet thickens. However, the finger length remains relatively constant in the case with plasma off, while it increases almost monotonically when the plasma is on. It is noted that the behavior of the inner diameter (in red squares) is similar regardless of the presence of plasma. In both instances, the values of d_{in} seem to plateau at $t \approx 3$ ms, which coincides with the time of maximum spreading in the case of plasma off. In addition, receding waves [such as those seen in Fig. 5(a) at $t = 7$ ms] begin to form at the rim and propagate inward. We determine that the inertial effect of the droplet spread ends when d_{in} plateaus. Further, l_f slightly decreases after the maximum spreading of the droplet in the absence of plasma. The formation of small ripples ($l_f/d_o = 0.15$) prior to maximum spreading in the absence of plasma results from the imbalance between inertial and capillary forces on the spreading front.[33,34] The instability does not grow in time since the inertial effects die out after maximum spreading.

On the other hand, the case with plasma exhibits finger growth during inertial effects as well as after the inertial spread has died out. A direct comparison between the two cases indicates that the finger growth rate during the inertial spreading is higher in the presence of plasma. This suggests that forces other than the inertial are involved. In fact, we observe that a bright plasma streamer forms between the electrode and the liquid at the moment of impact. The streamer formation is a nanosecond process, which takes place within the positive half of the AC cycle.[14] This initial streamer serves as a bridge through which a large number of charges are transferred to the droplet. The droplet is then subjected to Coulomb forces radially outward, resulting from the redistribution of charges. These forces are, however, circumferentially uneven due to the external electric field caused by the electrode. The added momentum to the initial spreading of the droplet favors the destabilization of the spreading front of the droplet and promotes the finger formation.

The effects of plasma on the wetting properties of the solid surface also play an important role in the droplet spreading and the fingering phenomenon. The wettability of the dielectric surface is denoted by the spreading parameter $S = \gamma_{SA} - \gamma_{SL} - \gamma_{LA}$, which is, in turn, defined by the surface tensions for the solid–air (SA), solid–liquid (SL), and liquid–air (LA) interfaces. As the polymer comes into contact with the plasma, its wettability increases.[25–28] The plasma intensity is stronger at the electrode and diminishes with increasing distance from the electrode. This renders a global gradient of increasing wettability (∇S) along the plasma stream direction. In addition, plasma ejections take place locally at the fingertips as the fingers develop and continue to occur as long as the finger maintains contact with the exposed electrode through liquid or through plasma streamers, as can be seen in the thermal images in Fig. 4. These ejections cause localized regions of increased wettability at the spreading front of the finger structures. The global and local gradients of wettability promote the development of the instability as follows. Upon impact, the droplet begins to spread radially out from the impinging point. As the liquid spreads away from the electrode, it encounters an adverse wettability gradient (global effect), i.e., the liquid faces a decrease in mobility, which is often a necessary condition for fingering, such as in Saffman–Taylor instability.[41–43] In addition, the local plasma discharges at the advancing fingertips increase the wettability of the surface, allowing the elongation of fingers after the inertial effects have died out.

Our observations hold some similarities with plasma-induced fingering instabilities reported in narrow gaps.[37–40] It is pointed out that while in our experiments the liquid was not confined, it was in the form of a thin film as a result of the droplet spreading. In addition, the plasma increases the wettability of the dielectric material and reduces the surface tension of the liquid, further promoting the droplet spreading. The spreading caused by inertial and Coulomb effect is then "self-confined" to the thin film, that is, no relaxation occurs in the direction normal to the plane. This thin film configuration is then a necessary condition for the finger instability to develop. Experiments were carried out (although omitted here) where sessile droplets at the electrode/dielectric interface were supplied with the same plasma intensities as those reported herein. This resulted in a decrease in the contact angle. However, no fingering was observed under such conditions, and recirculation occurred within the hemispherical droplet. The second point of comparison with the observations mentioned above[37–40] is the extent of instability evolution. In our case, the instability is restricted to the initial stage of finger formation, during which the fingers do not continuously grow or branch. This behavior is attributed to the expansion of the ionized gas phase as it heats over time. In a confined space, the plasma region continuously pushes through the liquid, causing a prolonged evolution of the instability.

B. Decoupling of inertial and electrical effects

To de-couple the inertial and electrical effects, the experiments were repeated such that the droplet impacted and spread fully on the dielectric material. This slightly delayed the transfer of the electrical charges on the droplet, and hence the onset of finger development. The sequences of photographs in Fig. 8 show the outcomes of two repetitions of the experiment. Droplets of 2.75 mm in diameter impacted the actuator 10.3 mm away from the edge of the electrode. Upon contact, the drops began to spread seemingly unperturbed by the plasma. However, as the spreading rim approached the high-voltage electrode, a single filamentary plasma structure (or streamer) appeared between the droplet and the electrode, giving rise to the onset of finger formation. The streamer is highlighted in red at the moment it is initially seen in Fig. 8, and the blue arrow indicates the direction normal to the

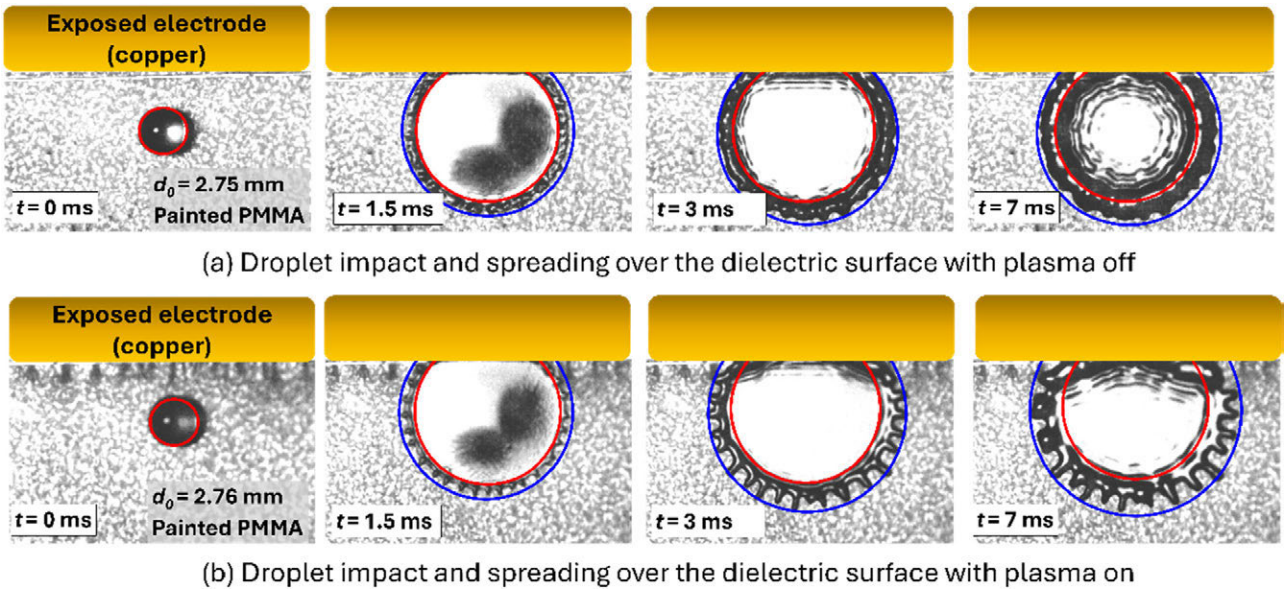

FIG. 5. Droplet impact and spreading over the PMMA dielectric surface at $We = 250$, (a) in the absence of plasma and (b) with surface DBD plasma discharge.

droplet's edge at which the streamer contacts it. The streamer appears as a thin white line in subsequent frames. The two sequences of frames in Fig. 8 show the same phenomenon with a slight variation in the point on the droplet (indicated as θ^* in terms of the polar coordinate convention established in Sec. II C) and the direction in which the streamer comes into contact with the droplet.

The images in the top row show that the streamer is formed and contacts the droplet at its closest point to the electrode ($\theta^* = 180°$) at $t = 1.66$ ms, when the droplet had nearly reached its maximum spreading size. Prior to this, the droplet spread evenly in all directions with its rim forming the characteristic ripples. At $t = 3$ ms, the streamer can be seen penetrating into the droplet. Simultaneously, the droplet's periphery is affected by the formation of an indentation at the point of contact ($\theta^* = 180°$) and a gradual transition from ripples to well-defined fingers in the furthermost parts of the droplet ($\theta^* \approx 0°$). The instability continues to grow for a few ms until the maximum length is reached at $t \approx 6$ ms. This finger formation is attributed entirely to electrical effects since inertial ones had already terminated. However, it appears that the flat shape of the droplet (or thin film) is a necessary condition for the finger stability to develop since liquid motion is restricted to a plane and momentum cannot be easily redistributed perpendicularly to the plane.

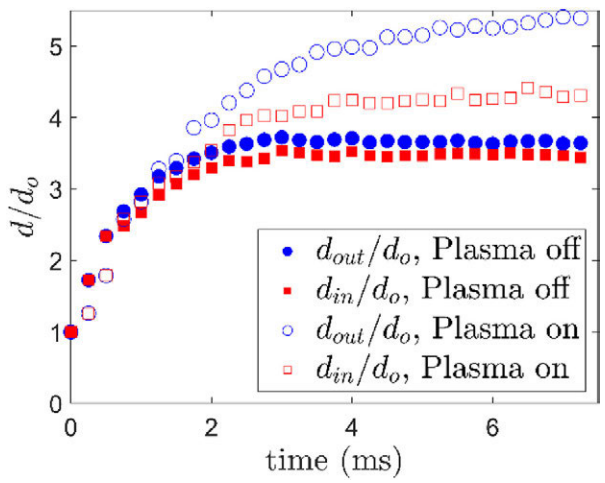

FIG. 6. The time evolutions of d_{in} (red square) and d_{out} (blue circle) normalized by d_o for plasma off (solid) and plasma on (hollow), respectively.

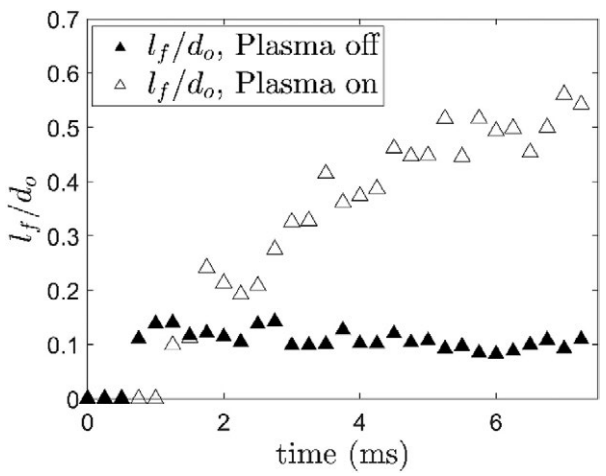

FIG. 7. The time evolutions of normalized average finger length ($l_f = (d_{out} - d_{in})/d_o$ for plasma off (solid triangle) and plasma on (hollow triangle), respectively.

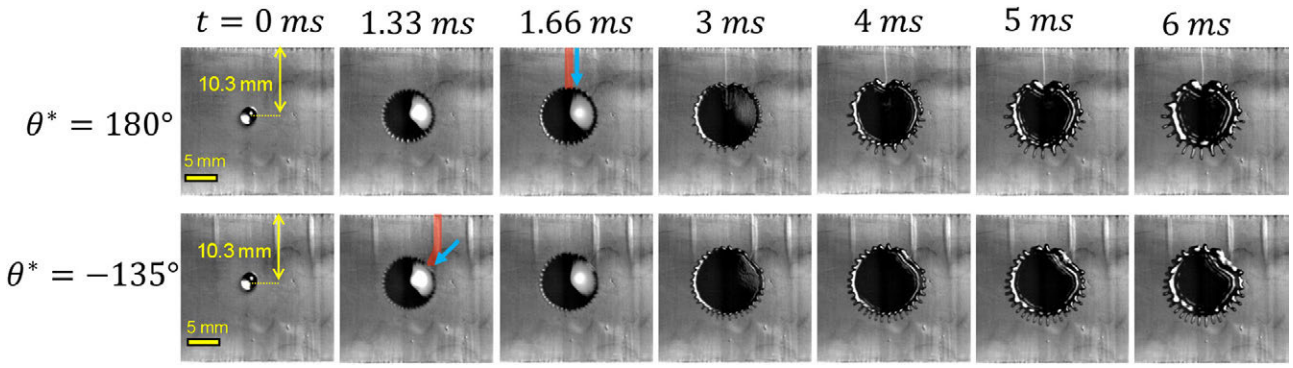

FIG. 8. Finger instability development on droplets impacting away from the exposed electrode.

The bottom row of photographs in Fig. 8 shows a similar effect but with the streamer contacting the droplet at an angle of $\theta^* \approx -135$ as highlighted in the frame corresponding to $t = 1.33$ ms. This behavior was caused by the deterioration of the dielectric material of the actuator. With prolonged use, slits form along the actuator due to the high temperatures (seen as vertical streaks in the lower row of images). These slits result in turn in localized regions of plasma intensity in the absence of the droplet. Upon impact, the droplet is reached by the already formed filamentary plasma structure in its vicinity ($\theta^* \approx -135$) rather than by a streamer formed after the impact. The interaction continues at the same location throughout the development of fingers, which also is considered to occur after the inertial effects have vanished. Similar to the previous case, the region of the droplet rim immediately in contact with the streamer presents an indentation and is void of finger structures. However, the finger length and slenderness distribution are asymmetrical. These effects are addressed next.

The distribution in finger length and slenderness is attributed to the local and global electric fields. In the first case of Fig. 8, the streamer acts in the same direction as the global electric field (as indicated by the blue arrow). As a result, the indentation and finger distribution are symmetric with respect to the $\theta = 0^\circ$ line such that the growth of fingers closer to the electrode is opposed by the electric field from the electrode as well as the local field of the streamer. In addition, the direction of the induced ionic wind can also resist the formation of fingers near the electrode and favor those away from it. The length and slenderness distribution of fingers in the second example is more complicated due to the direction of action of the streamer not being aligned with the main plasma discharge. After initial contact, the streamer remains acting upon the droplet at roughly the same location ($\theta = -135^\circ$) where the edge indentation (or rather a flattening) develops. The finger length then increases in the tangential direction away from the point of contact. Nonetheless, this distribution is not symmetrical with θ. It can be seen that both the finger length and slenderness on the side closer the electrode are hampered by effect of the electric field and ionic wind. On the other hand, the fingers farther from the electrode are long and thin, with the longest fingers still being near $\theta = 0^\circ$.

C. Characterization of droplet spreading and finger parameters

The onset of instability has been attributed to a combined effect of reduced mobility during the droplet spreading caused by the adverse wettability gradient normal to the electrode and the repelling Coulomb forces, which destabilize the rim of the spreading droplet. It has also been signaled that the thin film spreading is a necessary condition for the onset of the instability due to the restricted 2D fluid motion. Now, we address the relative roles of droplet inertia (characterized by We) and the electrical effects (identified by Bo_e) on the overall droplet spreading, and finger parameters such as finger length, spacing, and slenderness. To these effects, droplets of constant We (i.e., using the same needle size and released from the same h) were produced and allowed to impact the actuator at varying plasma intensities. Alternatively, a constant Bo_e can be achieved on droplets of the same size at a given plasma intensity. The We is then varied by adjusting h. The overall effects are presented in Fig. 9, where the left column of images shows droplets of $We = 40.87$ spreading over the dielectric surface of the DBD actuator at varying plasma intensities ($0 < Bo_e < 2.19$). On the other hand, the second column of images depicts droplets of a constant $Bo_e = 0.43$ over a range of We that varies from 40.87 to 490.5. The droplet contour is plotted in polar coordinates next to each image frame. The radial coordinate is normalized by the base radius r_b (average location of the finger troughs). The local minima and maxima are highlighted in red and blue dots, respectively.

The individual effects of We and Bo_e become clear from inspection of Fig. 9. It is seen that at a constant $We = 40.87$, the number of well-defined fingers increases. In fact, slender and well-defined fingers with maxima r/r_b values around 1.6 develop even with the lowest plasma intensity, in contrast to the case with no electrical actuation which displays no finger structures. In addition, the finger length becomes more uniform with increasing Bo_e. The ratio $\Theta = \theta_{fs}/\theta_r$, namely, the portion of the droplet's circumference occupied by fingers also increases with increasing Bo_e. The column on the right in Fig. 9 denotes the effects of We (release height h of the small droplet size) on the finger structures in a low plasma intensity ($Bo_e = 0.43$). The most obvious effects of an increased We are the degree of droplet spreading, and a substantial increase in the number of fingers (and hence a decrease in λ). The FFT analysis to determine the most probable wave number described in Sec. II C was applied to all the experimental cases. The results are discussed next.

Droplet spreading and finger size parameters are plotted against We and Bo_e in Fig. 10. The measured data at each We and Bo_e coordinate is shown by the circular markers, whereas the surface was generated by linear interpolation and is simply a visual aid. The degree of

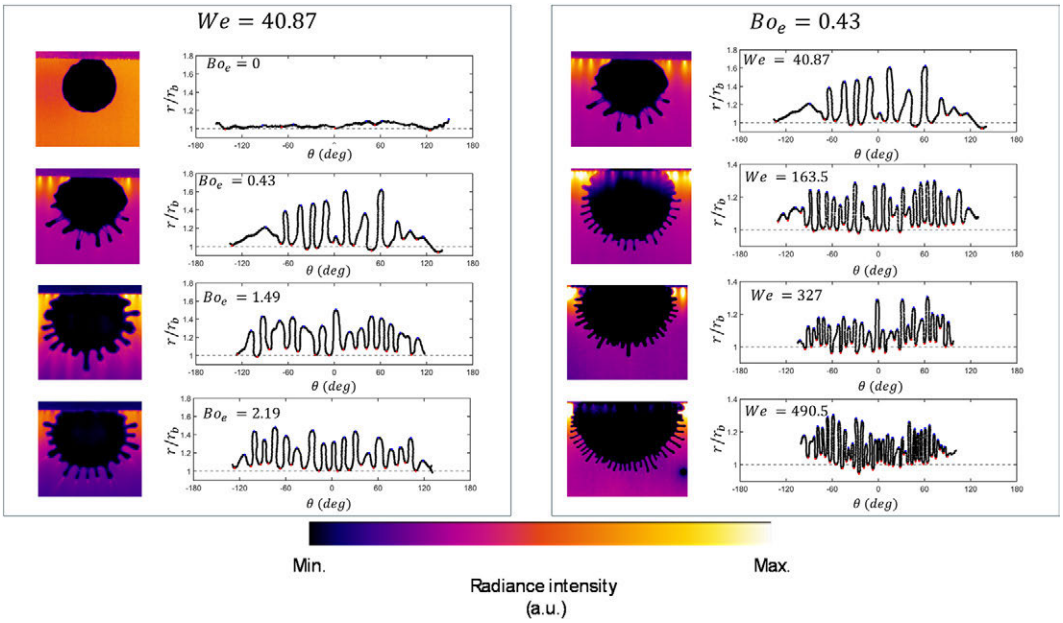

FIG. 9. Droplet spreading and finger formation under varying experimental parameters. Increasing *We* and Bo_e results in an increased number of fingers of smaller size. The top row of images shows the effect of increasing Bo_e at a fixed $We = 40.87$, whereas the bottom row shows the effect of increasing *We* at a constant $Bo_e = 0.22$.

droplet spreading is quantified by $\bar{r}/r_0$, i.e., the average radius value normalized by the droplet's initial radius. Its dependency on *We* and Bo_e is depicted in Fig. 10(a), where it becomes evident that droplet spreading increases with both *We* and Bo_e. In fact, the increase in $\bar{r}/r_0$ is nearly monotonic with respect to either variable. This dependency is further evidenced in Fig. 11, where the same normalized spreading factor is plotted against the product $We \times Bo_e^{1/4}$, suggesting a stronger dependency to *We*. The experimental data (for nonzero Bo_e) is approximated by a logarithmic curve fitting of the form ($R^2 = 0.9481$)

$$\bar{r}/r_0 = 2.31 \ln\left(We \times Bo_e^{1/4}\right) + 7.4. \tag{8}$$

This equation suggests that *We* plays a greater role in determining the maximum droplet spreading than Bo_e.

The normalized most probable wave number [N_m, Eq. (5)] is shown in Fig. 10(b). This is related to the number of fingers that would populate the entire circumference of the droplet (without the blockage from the electrode). The data ranges from mode 1 (no fingers) to 60 and in general, the data increases with both *We* and Bo_e. It is pointed out that in the absence of plasma ($Bo_e = 0$) no fingers are formed at low *We*. At the highest *We* (= 490.5) the rim of the droplet forms ripples which generate a relatively high N_m. However, these ripples do not meet the criteria of length and slenderness discussed next. At any fixed value of Bo_e, N_m increments with increasing *We*. Similarly, at a fixed *We*, N_m increases with increasing Bo_e. Similar to the spreading factor, the normalized number of fingers can be plotted against the product $We \times Bo_e^{1/4}$ as shown in Fig. 12 and approximated by the expression ($R^2 = 0.9041$)

$$N_m = 344.46 \times \exp\left[-0.0013\left(We \times Bo_e^{1/4}\right)\right] - 335 \times \exp\left[-0.002\left(We \times Bo_e^{1/4}\right)\right]. \tag{9}$$

Figure 10(c) shows the average finger length normalized by initial droplet size ($\bar{l}_f/r_0$). Note that the *We* and Bo_e axes are inverted with respect to the previous two plots for better visualization of the data. This plot indicates that the length of each finger can be as much as four times larger than the droplet's initial radius. Further, there is a significant increase in finger length when even a moderate plasma intensity is applied. This can be verified from the droplet profiles shown in Fig. 2. While the trends in Fig. 10(c) are not continuous, in general droplets at low *We* show longer fingers at the highest Bo_e values, on the other hand, as *We* increases, there is a diminishing of $\bar{l}_f$ in the higher Bo_e regime (see, for instance, the rightmost data point for $We = 490.5$, $Bo_e = 2.20$ which has a value of $\bar{l}_f/r_0 \approx 2$, considerably lower than its neighbors). This can be attributed to the larger degree of droplet spreading, which pushes the base of the fingers farther outward [note that the point mentioned earlier shows the largest $\bar{r}/r_0$ in Fig. 10(a)].

For further analysis, the average finger length was normalized by the mean radius after spreading ($\bar{l}_f/\bar{r}$) and is presented in Fig. 10(d). The results suggest that in general, for a fixed *We* a larger Bo_e yields longer fingers. Nonetheless, this effect is attenuated at larger *We* values. At the lowest values of *We* (<50) where the droplet carries little inertia, there is a significant progressive increase in finger length as the electrical effect becomes increasingly stronger. On the other hand, in highly inertial droplets ($We > 200$), there is only a significant increase in finger length between the case with no electricity and the lowest Bo_e (=0.43). After that, the value of $\bar{l}_f/\bar{r}$ plateaus with increasing Bo_e, suggesting that finger length is mostly dictated by droplet inertia.

Figure 13 shows additional parameters related to the finger structures. Note that the axes are oriented to better display the plotted data and that cases in which fingering was not identified ($Bo_e = 0$) are

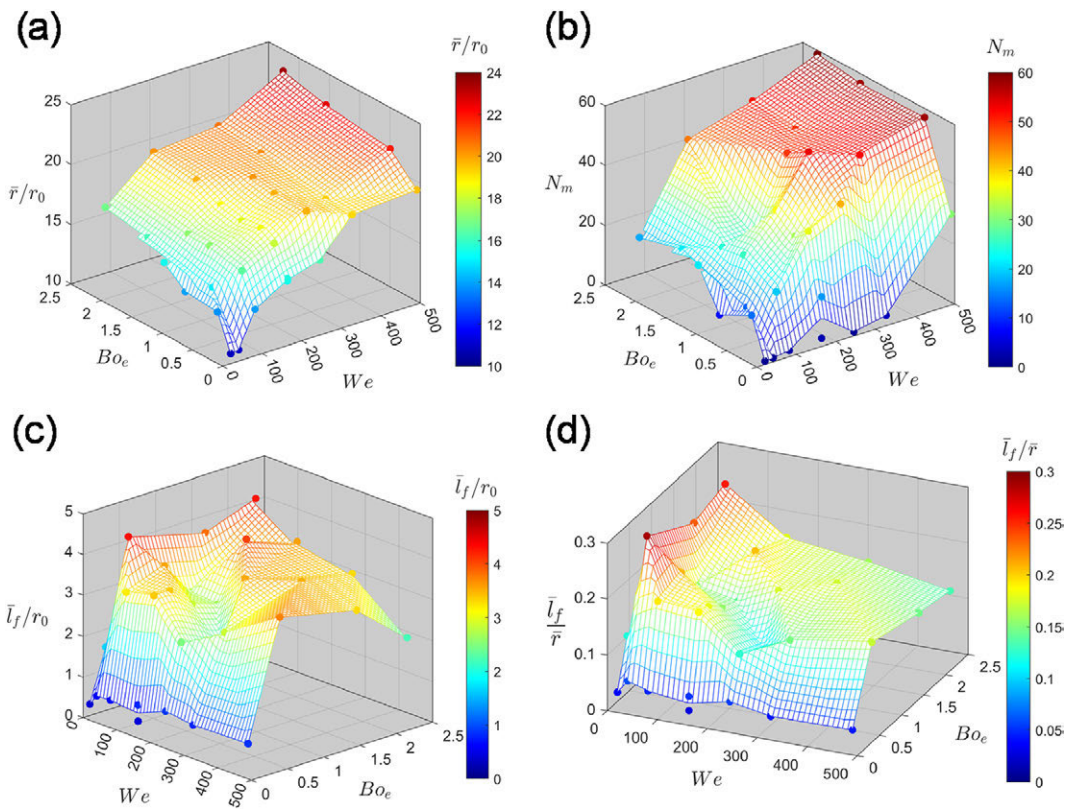

FIG. 10. Droplet and finger parameters (a) mean spreading radius, (b) normalized most probable mode, and the average finger length normalized by (c) r_0 and (d) $\bar{r}$, plotted against the nondimensional numbers *We* and Bo_e.

omitted. Figure 13(a) shows the wavelength λ calculated from Eq. (9). The plot shows that the largest values of λ occur at conditions of either low *We* or low Bo_e, on the other hand λ decreases at combinations of large *We* and Bo_e. A similar behavior is shown when plotting the angular spacing between fingers in Fig. 13(b), noting that the combination of Eqs. (5)–(7) yields $\lambda \propto \bar{r}s$.

Finger slenderness is herein quantified by $\bar{l}_f/\lambda$, and their values are plotted in Fig. 13(c). The data reveal a distinct dependence on *We*:

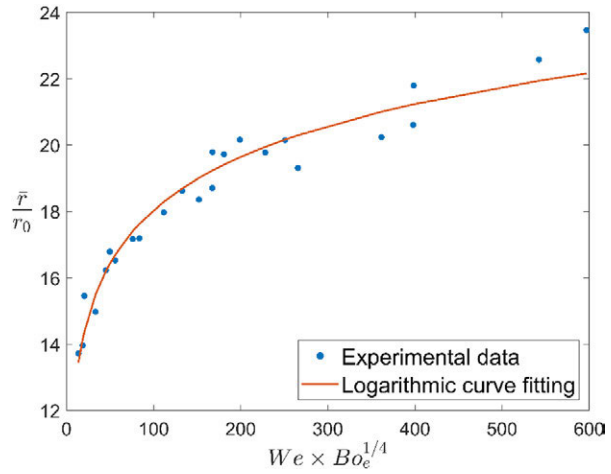

FIG. 11. Normalized droplet spreading $(\bar{r}/r_0)$ as a function of $We \times Bo_e^{1/4}$. A logarithmic curve fitting [Eq. (8)] is presented along with the experimental data.

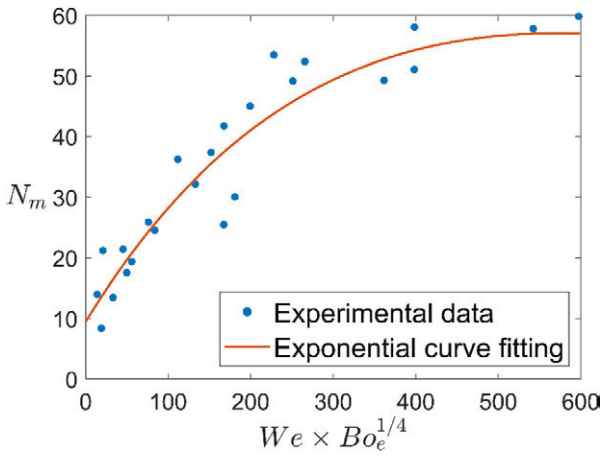

FIG. 12. Normalized number of fingers (N_m) as a function of $We \times Bo_e^{1/4}$. An exponential curve fitting [Eq. (9)] is presented along with the experimental data.

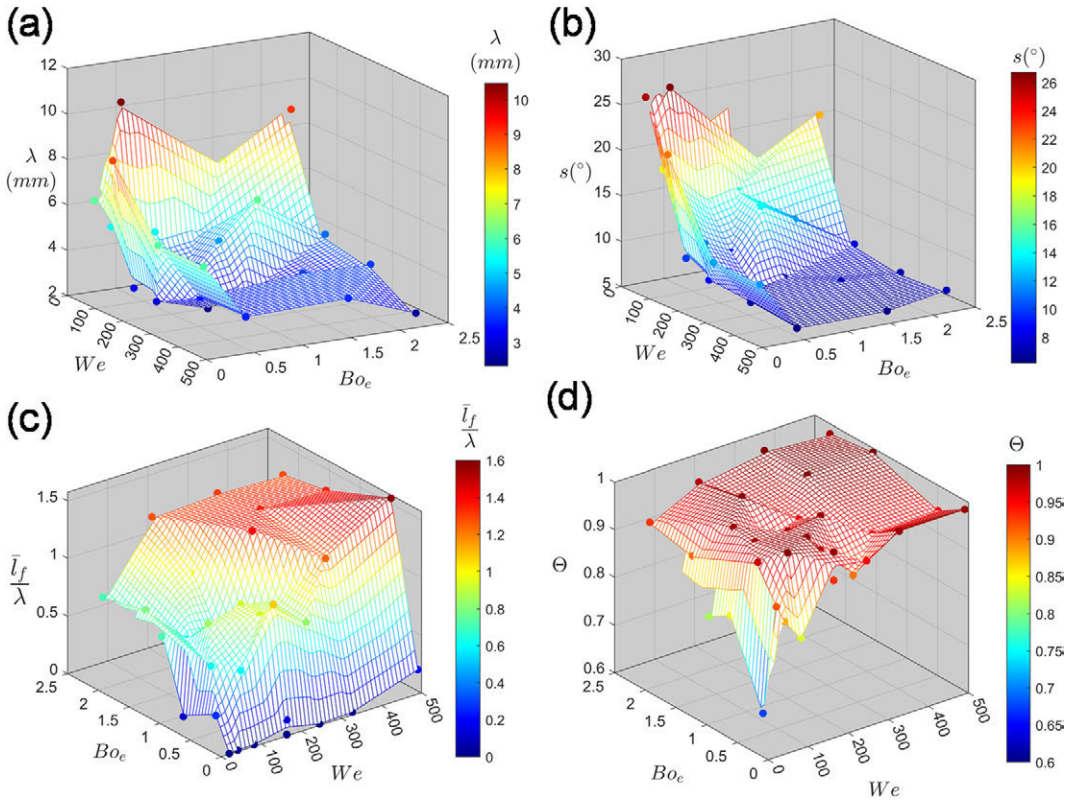

FIG. 13. Droplet and finger parameters (a) wavelength, (b) finger spacing, (c) finger slenderness, and (d) angular ratio plotted against the nondimensional numbers *We* and Bo_e.

in the presence of plasma ($Bo_e \neq 0$), droplets with higher *We* produce more slender finger structures. The dependence on Bo_e, on the other hand, is less straightforward. While in general, slenderness increases with Bo_e, the maximum values of $\bar{l}_f/\lambda$ at a given *We* occur at a moderate $Bo_e \approx 0.5$. Finally, the angular ratio Θ is presented in Fig. 13(d). It shows that the ratio occupied by fingers increases with both *We* and Bo_e, indicating that higher inertial and electrohydrodynamic effects not only promote the formation of more fingers but also allow them to cover a greater angular extent of the droplet perimeter.

D. Determination of fingering instability modes

Based on the droplet spreading and finger parameters presented above (number of fingers, finger length, and slenderness), we identified that in general, the data fell into five regimes. These regimes are described below and are illustrated in Figs. 14 and 15. Figure 14 shows the contours in Cartesian and polar coordinates of five droplet samples (one representative of each regime) along with the number of fingers (n_m) within θ_r for each case. Figure 15 displays a rough delimitation of each regime in a $We - Bo_e$ domain based on the investigated cases. Note that these group delimitations are somewhat subjective and can be verified by the reader for all experimental cases in Fig. 2. The characteristics of each group and *We*, Bo_e values are as follows:

I. **Low *We* and $Bo_e = 0$** (blue in Figs. 14 and 15). In the absence of plasma, droplets of relatively low inertia maintain a mostly circular shape upon impact with the surface. Droplets in this regime do not exhibit any evident finger formation, or a negligible ripple formation. Their perimeter has a relatively constant radius, i.e., the largest finger measurements are <10% of r_b. The sample droplet presented in Figs. 14 and 15 has a $We = 163.5$ and $Bo_e = 0$.

II. **High *We* and $Bo_e = 0$** (orange in Figs. 14 and 15). As the inertia of the droplet increases (still without plasma), some small ripples are formed at the rim during the spreading phase, as discussed earlier. The case presented ($We = 490.5$ and $Bo_e = 0$) exhibits 14 ripple structures (opposite to the slender fingers described in the previous section) with a maximum value of $r/r_b = 1.11$, the average inter-finger spacing is 11.4°.

III. **Low *We* and $Bo_e \neq 0$** (red in Figs. 14 and 15). This regime contained only droplets at the lowest *We* investigated (=20.4) at all the plasma intensities. Its main characteristic is the formation of a few well-defined fingers of irregular size scattered at irregular intervals. The sample case presented ($We = 20.4$, $Bo_e = 1.09$) exhibits three relatively well-defined fingers (at locations $\theta = -81°$, $-21°$, and 79° with an additional five protrusions intercalated around the edge. The eight fingers and protrusions have an average spacing of 26°.

IV. **Moderate *We* and $Bo_e \neq 0$** (magenta in Figs. 14 and 15). In general, these droplets exhibit 10–20 long fingers ($r/r_b \approx 1.5$) with inter-finger spacing of $s > 10°$. The case presented in Figs. 14 and

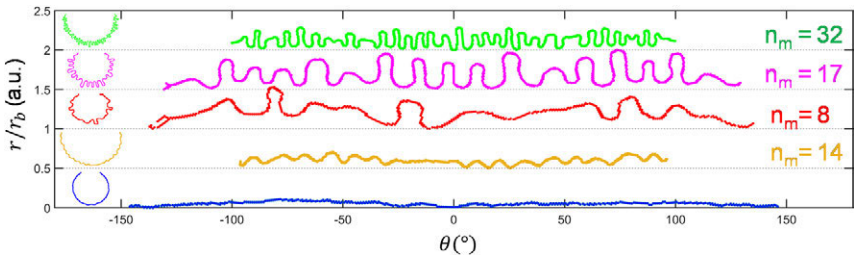

FIG. 14. Normalized droplet contours in polar coordinates (r/r_b) denoting the five instability modes identified in this study.

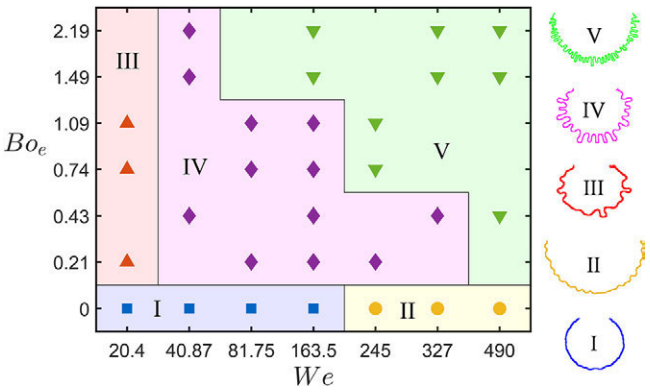

FIG. 15. Stability plot of the spreading and fingering regimes identified with representative samples. The regimes were characterized as I: low inertia and no electric stresses, minimum ripple formation. II: high inertia and no electric stresses, ripples are formed at the rim of the spreading droplet. III: low inertia with electrical stresses, some non-uniformly distributed fingers are formed. IV: moderate inertia with electrical stresses, relatively long and thick fingers are uniformly distributed around the droplet edge. V: high inertia and high electric stresses result in many small and thin fingers.

15 has 17 fingers with a $r_{max}/r_b = 1.48$ and an average spacing of 13.65°. This regime exhibits the longest fingers ($\bar{l}_f/r_0$, $\bar{l}_f/\bar{r}$) and occurs at moderate values of $We \times Bo_e$.

V. **Moderate to high We and $Bo_e \neq 0$** (green in Figs. 14 and 15). This spreading regime resembles the finger formations in Fig. 9 which contain >20 fingers of $r_{max}/r_b \approx 1.30$ and an average spacing of <10° between fingers. The case presented here ($We = 490$, $Bo_e = 1.49$) has 30 fingers with a $r_{max}/r_b = 1.25$ and an average spacing of 6.23°. This regime presents a large number of fingers, high slenderness numbers ($\bar{l}_f/\lambda$) and occurs at higher $We \times Bo_e$ values. Finger merging (similar to the observations by Thoroddsen and Sakakibara[34]) was often encountered in this regime. See for instance, the double finger structures in the top polar plot in Fig. 12 located at $\theta \approx -80°, -40°$, and $+50°$. These structures result from the merging of two distinct fingers in the early phase of spreading.

IV. CONCLUSIONS

We have presented experimental evidence highlighting the development of a fingering instability when water droplets impact the polymethyl methacrylate surface of a dielectric barrier discharge device during plasma actuation. The formation of fingers and their distribution proved to be a critical step in the subsequent breakup into secondary droplets, the development of high-intensity plasma streamers, and the droplet's evaporative dynamics. The development of the instability was attributed to reduced mobility due to an adverse wettability gradient on the surface caused by the plasma. Coulomb forces acting on the spreading droplet and localized plasma discharges on the fingertips aid to finger extension.

Droplet spreading and finger parameters were extracted from the droplets' contours in polar coordinates and contrasted against We and Bo_e. Droplet spreading and number of fingers increased nearly monotonically with increased We and Bo_e. Empirical relationships were drawn for these two parameters with respect to the product $We \times Bo_e^{1/4}$. Finger length and wavelength were highest at modest values $We \times Bo_e$, whereas finger slenderness ($\bar{l}_f/\lambda$) was highest at larger $We \times Bo_e$. In general, the data fell into five categories based on finger length, spacing, and distribution.

ACKNOWLEDGMENTS

This work was supported by the U.S. Department of Energy, Office of Science, Office of Fusion Energy Sciences under Award No. DE-SC0024663.

AUTHOR DECLARATIONS

Conflict of Interest

The authors have no conflicts to disclose.

Author Contributions

Jorge Ahumada Lazo: Data curation (equal); Formal analysis (equal); Investigation (equal); Methodology (equal); Validation (equal); Visualization (equal); Writing – original draft (equal). **Yang Liu:** Conceptualization (equal); Formal analysis (equal); Funding acquisition (equal); Investigation (equal); Methodology (equal); Project administration (equal); Resources (equal); Software (equal); Supervision (equal); Validation (equal); Visualization (equal); Writing – review & editing (equal).

DATA AVAILABILITY

The data that support the findings of this study are available from the corresponding author upon reasonable request.

REFERENCES

[1]P. J. Bruggeman, M. J. Kushner, B. R. Locke, J. G. E. Gardeniers, W. G. Graham, D. B. Graves, R. C. H. M. Hofman-Caris, D. Maric, J. P. Reid, E. Ceriani, D. Fernandez Rivas, J. E. Foster, S. C. Garrick, Y. Gorbanev, S. Hamaguchi, F. Iza, H. Jablonowski, E. Klimova, J. Kolb, F. Krcma, P. Lukes, Z.

MacHala, I. Marinov, D. Mariotti, S. Mededovic Thagard, D. Minakata, E. C. Neyts, J. Pawlat, Z. L. Petrovic, R. Pflieger, S. Reuter, D. C. Schram, S. Schröter, M. Shiraiwa, B. Tarabová, P. A. Tsai, J. R. R. Verlet, T. von Woedtke, K. R. Wilson, K. Yasui, and G. Zvereva, "Plasma–liquid interactions: A review and roadmap," Plasma Sources Sci. Technol. **25**(5), 053002 (2016).
[2]J. C. Laas, R. T. Garrod, E. Herbst, A. O. Elnabawy, J. A. Herron, J. Scaranto, J. Hedberg, S. Baldelli, C. Leygraf, G. Oinuma, G. Nayak, Y. Du, and P. J. Bruggeman, "Controlled plasma–droplet interactions: A quantitative study of OH transfer in plasma–liquid interaction," Plasma Sources Sci. Technol. **29**(9), 095002 (2020).
[3]G. Nayak, G. Oinuma, Y. Yue, J. S. Sousa, and P. J. Bruggeman, "Plasma–droplet interaction study to assess transport limitations and the role of OH, O, H, O2(a 1Δg), O3, He(23 S) and Ar(1s 5) in formate decomposition," Plasma Sources Sci. Technol. **30**(11), 115003 (2021).
[4]Y. Liu, C. Kolbakir, H. Hu, A. Y. Starikovskiy, R. B. Miles, and H. Hu, "An experimental study on the thermal characteristics of NS-DBD plasma actuation and application for aircraft icing mitigation," Plasma Sources Sci. Technol. **28**(1), 014001 (2019).
[5]Y. Sui, C. A. Zorman, and R. M. Sankaran, "Plasmas for additive manufacturing," Plasma Processes Polym. **17**(5), 2000009 (2020).
[6]P. Vanraes and A. Bogaerts, "The essential role of the plasma sheath in plasma–liquid interaction and its applications—A perspective," J. Appl. Phys. **129**(22), 220901 (2021).
[7]R. Akolkar and R. M. Sankaran, "Charge transfer processes at the interface between plasmas and liquids," J. Vac. Sci. Technol. A **31**(5), 050811 (2013).
[8]A. M. Worthington, "On the forms assumed by drops of liquids falling vertically on a horizontal plate," Proc. R. Soc. London **25**, 261–272 (1877).
[9]C. Josserand, S. T. T. Thoroddsen, C. Josserand, and S. T. Thoroddsen, "Drop impact on a solid surface," Annu. Rev. Fluid Mech. **48**(1), 365–391 (2016).
[10]M. Rein, "Phenomena of liquid drop impact on solid and liquid surfaces", Fluid Dyn. Res. **12**, 61 (1993).
[11]S. Chandra and C. T. Avedisian, "On the collision of a droplet with a solid surface", Proc. R. Soc. A **8**, 1098 (1991).
[12]S. Moghtadernejad, C. Lee, and M. Jadidi, "An introduction of droplet impact dynamics to engineering students," Fluids **5**(3), 107 (2020).
[13]A. Mohammad Karim, "Physics of droplet impact on various substrates and its current advancements in interfacial science: A review," J. Appl. Phys. **133**(3), 030701 (2023).
[14]N. Benard and E. Moreau, "Electrical and mechanical characteristics of surface AC dielectric barrier discharge plasma actuators applied to airflow control," Exp. Fluids **55**, 1846 (2014).
[15]M. Kotsonis, "Diagnostics for characterisation of plasma actuators," Meas. Sci. Technol. **26**(9), 092001 (2015).
[16]M. Kotsonis, S. Ghaemi, L. Veldhuis, and F. Scarano, "Measurement of the body force field of plasma actuators," J. Phys. D: Appl. Phys. **44**(4), 045204 (2011).
[17]Y. Kaneko, H. Nishida, and Y. Tagawa, "Visualization of the electrohydrodynamic and thermal effects of AC-DBD plasma actuators of plate- and wire-exposed electrodes," Actuators **11**(2), 38 (2022).
[18]T. C. Corke, C. L. Enloe, and S. P. Wilkinson, "Dielectric barrier discharge plasma actuators for flow control," Annu. Rev. Fluid Mech. **42**, 505–529 (2010).
[19]T. C. Corke, M. L. Post, and D. M. Orlov, "Single dielectric barrier discharge plasma enhanced aerodynamics: Physics, modeling and applications," Exp. Fluids **46**(1), 1–26 (2009).
[20]C. L. Enloe, T. E. McLaughlin, R. D. VanDyken, K. D. Kachner, E. J. Jumper, T. C. Corke, M. Post, and O. Haddad, "Mechanisms and responses of a single dielectric barrier plasma actuator: Geometric effects," AIAA J. **42**(3), 595–604 (2004).
[21]C. Kolbakir, H. Hu, Y. Liu, and H. Hu, "An experimental study on different plasma actuator layouts for aircraft icing mitigation," Aerosp. Sci. Technol. **107**, 106325 (2020).
[22]Y. Liu, C. Kolbakir, H. Hu, and H. Hu, "A comparison study on the thermal effects in DBD plasma actuation and electrical heating for aircraft icing mitigation," Int. J. Heat Mass Transfer **124**, 319–330 (2018).
[23]Y. Liu, C. Kolbakir, H. Hu, X. Meng, and H. Hu, "An experimental study on the thermal effects of duty-cycled plasma actuation pertinent to aircraft icing mitigation," Int. J. Heat Mass Transfer **136**, 864–876 (2019).
[24]F. Rodrigues, M. Abdollahzadehsangroudi, J. Nunes-Pereira, and J. Páscoa, "Recent developments on dielectric barrier discharge (DBD) plasma actuators for icing mitigation," Actuators **12**(1), 5 (2022).
[25]M. Lehocký, H. Drnovská, B. Lapčíková, A. M. Barros-Timmons, T. Trindade, M. Zembala, and L. Lapčík, "Plasma surface modification of polyethylene," Colloids Surf., A **222**, 125–131 (2003).
[26]S. Han, Y. Lee, H. Kim, G.-H. Kim, J. Lee, J.-H. Yoon, and G. Kim, "Polymer surface modification by plasma source ion implantation," Surf. Coat. Technol. **93**, 261 (1997).
[27]R. Morent, N. De Geyter, T. Desmet, P. Dubruel, and C. Leys, "Plasma surface modification of biodegradable polymers: A review," Plasma Processes Polym. **8**(3), 171–190 (2011).
[28]Q. Wen, Y. Shi, Y. Li, G. Yang, Z. Liu, Y. Fu, Z. Zhang, L. Zhang, X. Wang, and X. Jiang, "Negative effects of SDBD plasma anti-/de-icing method for wind turbine blades," Appl. Surf. Sci. **688**, 162341 (2025).
[29]K. S. Wong, N. S. L. Chew, M. Low, and M. K. Tan, "Plasma-activated water: Physicochemical properties, generation techniques, and applications," Processes **11**, 2213 (2023).
[30]Y. Gao, K. Francis, and X. Zhang, "Review on formation of cold plasma activated water (PAW) and the applications in food and agriculture," Food Res. Int. **157**, 111246 (2022).
[31]M. Shaji, A. Rabinovich, M. Surace, C. Sales, and A. Fridman, "Physical properties of plasma-activated water," Plasma **6**(1), 45–57 (2023).
[32]J. A. Lazo, P. Lelikov, M. S. B. Sarwar, and Y. Liu, "Effects of water droplet impact on the flow characteristics in dielectric barrier discharge plasma actuation," in *Proceedings of the ASME 2024 International Mechanical Engineering Congress and Exposition. Volume 8: Fluids Engineering* (ASME, 2024).
[33]H. Marmanis and S. T. Thoroddsen, "Scaling of the fingering pattern of an impacting drop," Phys. Fluids **8**(6), 1344–1346 (1996).
[34]S. T. Thoroddsen and J. Sakakibara, "Evolution of the fingering pattern of an impacting drop," Phys. Fluids **10**(6), 1359–1374 (1998).
[35]S. E. May and J. V. Maher, "Fractal dimension of radial fingering patterns," Phys. Rev. A **40**, 1723 (1989).
[36]J. M. Zhang, E. Q. Li, and S. T. Thoroddsen, "Fine radial jetting during the impact of compound drops," J. Fluid Mech. **883**, A46 (2020).
[37]H. Y. Chu and H. K. Lee, "Evolution of the plasma bubble in a narrow gap," Phys. Rev. Lett. **107**(22), 225001 (2011).
[38]S. Y. Hou and H. Y. Chu, "Saffman–Taylor-like instability in a narrow gap induced by dielectric barrier discharge," Phys. Rev. E **92**(1), 013101 (2015).
[39]L. Potočňáková, P. Synek, and T. Hoder, "Viscous droplet in nonthermal plasma: Instability, fingering process, and droplet fragmentation," Phys. Rev. E **101**(6), 063201 (2020).
[40]L. Kuthanová and T. Hoder, "Dynamics of microflow at the plasma–liquid interface," Sci. Rep. **12**(1), 16665 (2022).
[41]P. G. Saffman and G. Taylor, "The penetration of a fluid into a porous medium or Hele-Shaw cell containing a more viscous liquid," Proc. R. Soc. London, Ser. A **245**, 312–329 (1958).
[42]A. Pouplard and P. A. Tsai, "Controlling viscous fingering instabilities of complex fluids," Sci. Rep. **14**(1), 2338 (2024).
[43]O. K. Matar and S. M. Troian, "The development of transient fingering patterns during the spreading of surfactant coated films," Phys. Fluids **11**(11), 3232–3246 (1999).